ACS APPLIED POLYMER MATERIALS

pubs.acs.org/acsapm

Article

Multi-Stimuli Responsive Soft Actuator with Locally Controllable and Programmable Complex Shape Deformations

Jingyi Zhang, Yu Wang,* Yuxi Sun, Shuaishuai Sun, Zhenbang Xu, Jun Li, Ji Li, and Xinglong Gong*

Cite This: *ACS Appl. Polym. Mater.* 2023, 5, 6199−6211

Read Online

ACCESS | Metrics & More | Article Recommendations | Supporting Information

ABSTRACT: The soft actuators capable of responding to multiple stimuli and adapting to changing environments have attracted growing interest in the flexible multifunctional materials. However, how to achieve high degree of freedom (DoF), precise control, and complex shape transformation of the multi-stimuli responsive soft actuator, still remains challenging. Here, we report a multi-responsive soft actuator with various controllable sophisticated deformations by integrating a magnetically sensitive elastomer (MSE) with a liquid crystal elastomer (LCE). Through regulating the stimuli strength and the geometrical dimensions and material parameters of elastomers, the bending angle and curling curvature of the actuator are accurately controlled ranging from 0 to 58.9° and from 0.23 to 1.29 cm^{-1}, respectively. The facile material-structural synergistic design drives the complex 3D shape deformations (e.g., bidirectional bending, shrinkage/bending, rolling/bending, and twisting/bending) of the actuator. More importantly, due to its photosensitive characteristics, the shape-morphing of the actuator can be manipulated locally and sequentially, which markedly enriches the DoFs. The flower-shaped actuator displays multiple deformation modes, and the hand-shaped actuator transforms between 8 gestures under the control of laser and magnetic field, proving that the multi-responsive soft actuators have great application potentials in future bioengineering, soft manipulators, and flexible electronics.

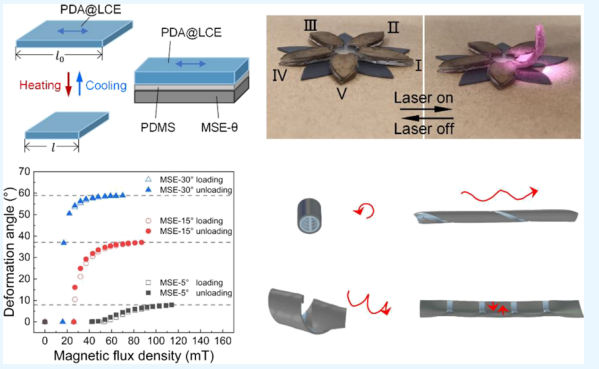

KEYWORDS: *multi-stimuli responsive actuator, smart material, magnetic, shape morphing, photothermal*

1. INTRODUCTION

Animals and plants in nature are intelligently responsive to changing environments, displaying diverse deformations and motions to survive and evolve.[1,2] Inspired by these living organisms, various soft actuators that can respond to external stimuli, especially light,[3] humidity,[4] chemical fuels,[5] electrical,[6] and magnetic field[7] have been developed to benefit soft robotics,[8] flexible electronics,[9] and biomedical fields.[10,11] Compared with the soft actuators with single responsive capability to stimulus, the multi-stimuli responsive soft actuators can meet the multifunctional requirements, having drawn a great deal of attention.[12,13] Weng et al. explored the different 3D shape deformations of the light/humidity-triggered graphite paper/polymer actuator and demonstrated the application for manipulating objects.[14] Du et al. designed the temperature-responsive hydrogel-based millirobots embedded with magnetic particles, which showed crawling, swinging, and rolling and shrinkingly went through a narrow tube.[15] However, despite the advantageous performances of programmable deformation, transformable locomotion, and adaptability, the multi-stimuli responsive soft actuators capable of precise, complex, and multimodal deformations under simple control yet remain challenging.[16,17]

Magnetically sensitive elastomers (MSEs) consists of hard/soft-magnetic fillers and polymeric material matrices.[18] After the application of an external magnetic field, MSE exhibits macroscopic magnetodeformation due to the interaction between the magnetized particles and between the particles and the matrix.[19] Moreover, the magnetodeformation is wirelessly controlled, fast, and reversible.[20] Especially, the adjustable magnetodeformation of MSE allows it to be outstanding candidates for soft actuators.[21] By replacing the matrix of MSEs with responsive polymers, the multi-stimuli responsive soft actuators have been investigated to pursue complex multimode deformation.[22−24] Kuang et al. exploited a magnetic dynamic polymer composite by embedding hard-magnetic particles in a thermally responsive polymer network, enabling reconfigurable shape morphing.[25] Deng et al. reported a laser heating and magnetic reprogramming strategy to re-

Received: April 24, 2023
Accepted: July 7, 2023
Published: July 21, 2023

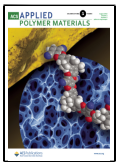

https://doi.org/10.1021/acsapm.3c00858
ACS Appl. Polym. Mater. 2023, 5, 6199−6211

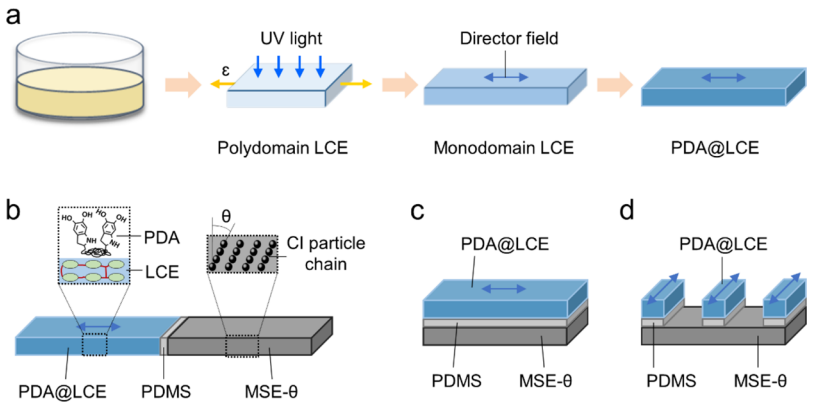

Figure 1. (a) Fabrication steps of the PDA@LCE. (b) In-plane stacking PDA@LCE/MSE. (c) PDA@LCE/MSE with the *z* stacking configuration. (d) PDA@LCE/MSE with the *z*-like stacking configuration.

align the localized magnetic particles encapsulated in a phase change polymer, achieving multiple 3D shaping modes under the same magnetic field.[26] For the above methods, magnetization reprogramming is requisite, which is not preferred for practical engineering applications. In addition, the morphing modes of these multi-stimuli responsive soft actuators are invariably based on magnetically induced bending,[27,28] which still hinders the realization of the complex deformation including bidirectional shrinkage and combined movements (e.g., contraction while bending). Liquid crystal elastomers (LCEs) can show reversible contraction or out-of-plane bending under the stimulus resources (heat or light)[29−33] and are widely used in artificial muscles,[34] photographic optics,[35] microfluidics,[36] etc. Zhang et al. proposed the bimorph actuators leveraging the thermal triggered deformation of LCEs and the magnetically induced bending of MSE, which exhibited complex shape-morphing more than bending.[37,38] However, the magnetic and thermal control are both nonlocal, resulting in that the actuator with a certain configuration has only four deformation modes when separately or conjunctly stimulated.[38] However, high deformation degree of freedoms (DoFs) of the multi-stimuli responsive soft actuators are also highly demanded.[39]

Herein, through coating the photo-thermal conversion material polydopamine (PDA) on the LCE and then integrating it with the MSE, we present a light/thermal/magnetic multiple responsive soft actuator (PDA@LCE/MSE) with controllable and programmable complex multimode deformation. The temperature- and magnetic-field-related material parameters and basic mechanical properties of PDA@LCE/MSE are characterized by a series of physical and chemical experiments. The deformation and actuation properties of each component are observed under different physical fields. The deformation behavior of PDA@LCE/MSE with different configurations under magnetic field and temperature field is investigated by experiments and the finite element method, and the deformation mechanism is analyzed. Finally, based on PDA@LCE/MSE, flower-like and hand-like actuators are developed to explore its potential applications in flexible electronic and soft manipulators.

2. EXPERIMENTAL SECTION

2.1. Materials. 4-*bis*-[4-(3-Acryloyloxypropyloxy) benzoyloxy]-2-methylbenzene (RM257) was purchased from Yesheng Chemical Technology Co., Ltd. 2-Hydroxy-4′-(2-hydroxyethoxy)-2-methylpropiophenone (HHMP), pentaerythritol tetrakis (3-mercaptopropionate) (PETMP), 2,2-(ethylenedioxy) diethanethiol (EDDET), dipropylamine (DPA), toluene, PDA hydrochloride, and tris base were purchased from Aladdin. The poly(dimethylsiloxane) (PDMS) precursor and curing agent (Sylgard 184) were purchased from Dow Corning. Carbonyl iron (CI) particles (CN-type) were bought from BASF Aktiengesellschaft. The mean diameter of the near-spherical particles was 7 μm. All the chemicals were used directly without further purification.

2.2. Fabrication of LCE. The LCEs are fabricated by a two-step thiol-acrylate reaction proposed by Yakacki et al.[40] In the first step, polydomain LCEs are prepared by the Michael addition reaction. The monomer solution is prepared with an excess of 15% acrylate groups relative to thiol groups. The diacrylate mesogen of RM257 (0.5 g) and the photoinitiator of HHMP (0.0035 g) are dissolved to toluene (0.25 mL) at 80 °C for 20 min. When the solution is cooled to room temperature, PETMP (0.036 g), a tetra-functional thiol cross-linking monomer, EDDET (0.10775 g), a di-thiol monomer, and diluted catalyst solution (0.142 g, diluting DPA with toluene at a ratio of 1:100) are immediately added and vigorously mixed. Then, the solution is degassed in a vacuum chamber to remove air bubbles and allowed to react for 12 h at room temperature. After that, the solution is heated at 80 °C for 24 h in the vacuum chamber and the polydomain LCE is fabricated.

The two ends of the polydomain LCE are taped to the fixed end and the sliding block of the sliding table, respectively. The polydomain LCE is stretched through moving the sliding block, followed by being irradiated for 10 min under a UV lamp (250 mW/cm^2, 365 nm/10 W, Starlight professional UV, China) with the sliding table. As shown in Figure 1a, the prestretching causes the mesogens in the LCE to align along the stretching direction (director field direction). The light further cross-links the matrix, thus fixing the mesogen alignment.

The ratio of the monodomain LCE length to the original polydomain LCE length is the pre-stretch. During each fabrication, the mass of the components and the volume of the glass culture dish are constant, which ensures that the thickness of the polydomain LCE is the same each time. Based on the volumetric noncompressibility, for polydomain LCEs with the same thickness, the thickness of the prepared monodomain LCEs is determined by the pre-stretch. Therefore, the thickness of the monodomain LCEs can be controlled by pre-stretch. The pre-stretch is 200% in the experiments unless specified.

2.3. Fabrication of PDA@LCE. PDA hydrochloride (0.2 g) and tris base (0.1 g) are dissolved in 100 mL of water. The monodomain LCEs are immersed in the solution and stirred for 24 h. The resultant PDA@LCEs are washed with deionized water three times and air-dried. Figure S1 exhibits polydomain LCE, monodomain LCE, and PDA@LCE samples at room temperature. The polydomain LCE is opaque while the monodomain LCE is transparent. When monodomain LCE is coated with PDA, its color becomes darker.

https://doi.org/10.1021/acsapm.3c00858
ACS Appl. Polym. Mater. 2023, 5, 6199−6211

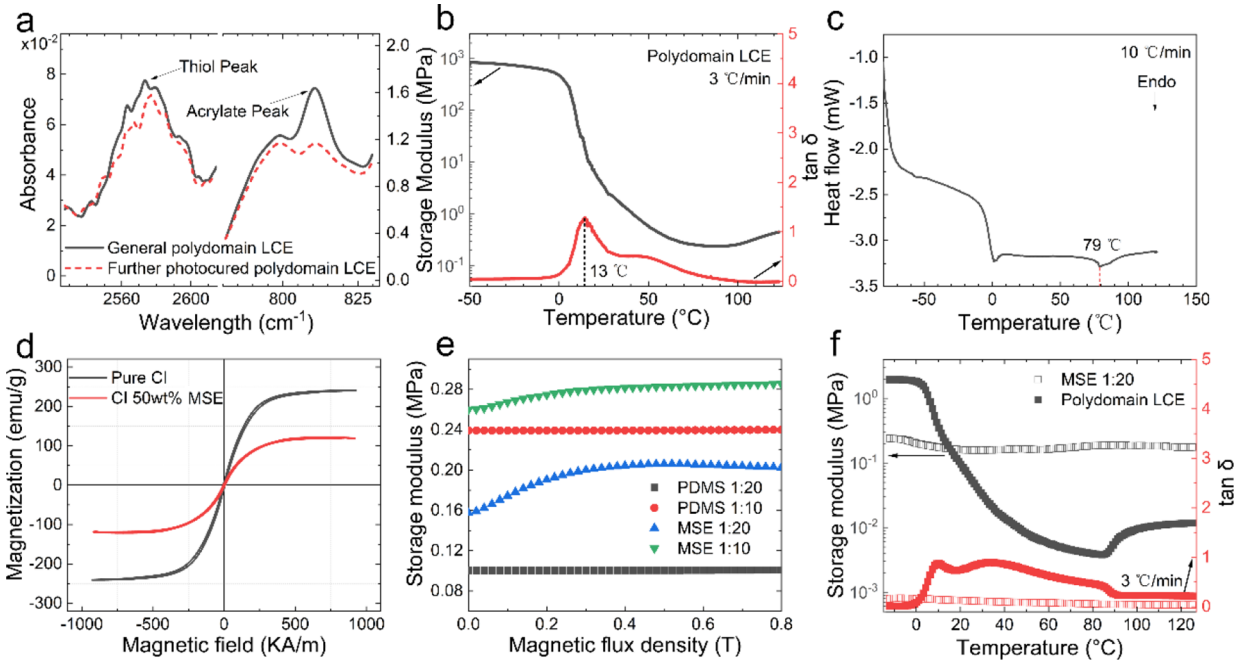

Figure 2. (a) FTIR spectra of general polydomain LCE and further photocured polydomain LCE. (b) Tensile thermomechanical properties of polydomain LCE. (c) DSC results for polydomain LCE. (d) Magnetization curves of CI and MSE with CI content of 50 wt %. (e) Magnetorheological characteristics of PDMS and MSE with different curing agent contents. (f) Effect of temperature on shear storage modulus and tan δ of the polydomain LCE and MSE.

2.4. Fabrication of PDMS and MSE. The curing agent and PDMS precursor at 1:20 and 1:10 are mixed thoroughly. The mixture is poured into molds followed by being placed in a vacuum chamber to remove air bubbles. Then, the mixture is cured at 100 °C for 20 min. After demolding, PDMS is fabricated.

The curing agent and PDMS precursor at 1:20 and 1:10 are first mixed. The CI particles are added in the mixture according to mass ratio 1:1. Next, the mixture is stirred and transferred in molds followed by being degassed for 20 min. Then, the matrix is placed on a heating plate with 100 °C together in a pre-structured magnetic field of 1 T for 20 min. Finally, the cured MSE is separated from the mold. Through varying the direction of the pre-structured magnetic field, the different MSEs with particle chain orientation angles of 5, 15, and 30° are prepared.[41] They are named MSE-5°, MSE-15°, and MSE-30°, respectively.

2.5. Fabrication of PDA@LCE/MSE. To make in-plane stacking PDA@LCE/MSE (Figure 1b), the pre-made PDA@LCE and MSE are cut to suitable sizes followed by being stuck onto the silicon wafer with double-side tape. The gaps between the PDA@LCE and MSE are filled by the mixture of the PDMS precursor and curing agent at 20:1. After 5 h of curing at 50 °C, the PDA@LCE/MSE is separated from the double-side tape. Finally, the excess PDMS of the PDA@LCE/MSE is removed with scissors.

The pre-made PDA@LCE is stuck onto the MSE by the mixture of the PDMS precursor and the curing agent at 20:1. After 5 h of heating at 50 °C, the z stacking PDA@LCE/MSE is fabricated (Figure 1c).

2.6. Characterization and Test. Fourier transform infrared spectra for LCE are obtained by FTIR spectroscopy (FTIR, NICOLET iS10, Thermo Fisher Scientific). Differential scanning calorimetry for polydomain LCE is performed with the heating rate of 10 °C/min (DSC 204 F1, NETZSCH). The thermomechanical properties of polydomain LCE (dimension: about 9.6 mm × 4.3 mm × 1 mm) are measured by dynamic mechanical analysis (DMA, Q800, TA Instruments, USA). The sample is tested in tensile mode and cycled at 0.2% strain at 1 Hz from −50 to 125 °C. The mesogen alignment of monodomain LCE is observed through 2D X-ray diffraction (XRD, Xeuss 2.0, Xenocs, France) and polarized optical microscopy (POM, Olympus bx51, Japan). The hysteresis loops of CI particles and MSE are tested by a magnetic property measuring system (HyMDC Metis, Leuven, Belgium). The magnetorheological properties and thermomechanical properties of MSE (dimension: about Φ 20 mm × 0.85 mm) are measured by a rheometer (Physica MCR 302, Anton Paar Co., Austria) with a magneto-controllable accessory. The samples are sheared at a frequency of 1 Hz with an amplitude of 0.2%. The pre-compression force is 5 N.

The tensile experiments of the samples are performed on an electroforce dynamic system (DMA, TA ElectroForce 3200, TA Instruments, USA). The displacement rate is 0.2 mm/s. The dimensions of polydomain LCE, monodomain LCE, monodomain LCE at 100 °C, and PDA@LCE for tensile experiment are 10 mm × 4.31 mm × 1 mm, 10 mm × 5 mm × 0.54 mm, 8.3 mm × 5.5 mm × 0.87 mm, and 10 mm × 5.5 mm × 0.53 mm, respectively. The tensile test of the monodomain LCE is performed along its director field direction. Based on the national standard GB/T528-2009, the size of MSE and PDMS for tensile experiment is 20 mm × 5 mm × 0.95 mm. The thickness of the sample is measured using a vernier caliper, and the average of the three measurements is taken as the final thickness of the sample. The instrument error of the vernier caliper is 0.02 mm. The tensile test for each sample is repeated three times.

The tensile and peeling test of PDA@LCE/MSE are conducted with a constant drawing speed of 0.2 and 0.5 mm/s on the DMA. The thermal expansion coefficient of monodomain LCE is measured by a thermomechanical analyzer (TMA 402F3, NETZSCH, Germany).

2.7. Generation of Magnetic and Thermal Stimuli. To evaluate the heat-induced deformation of PDA@LCE, the sample is placed on a hot plate (JF966-100, JFTOOLS, China) at 100 °C. One and two electromagnets (XDA-120/70, Yueqing Xingda Electric Co., Ltd., China) are employed to generate gradient and uniform magnetic fields, respectively. The DC power supply (ITECHIT6724) controls the magnitude of the magnetic field.

2.8. Actuating Force and Temperature of PDA@LCE under Laser Irradiation. The PDA@LCE (dimension: about 10 mm × 6 mm) is preloaded with 0.01 N using the DMA. A near-infrared laser (NIR, 808 nm, SKY laser, China) is applied to the sample. The maximum light intensity of the laser is 2 W/cm^2. The actuation force is recorded by the load cell of the DMA. The surface temperature of the sample is measured by an infrared camera (ImageIR 8325).

https://doi.org/10.1021/acsapm.3c00858
ACS Appl. Polym. Mater. 2023, 5, 6199−6211

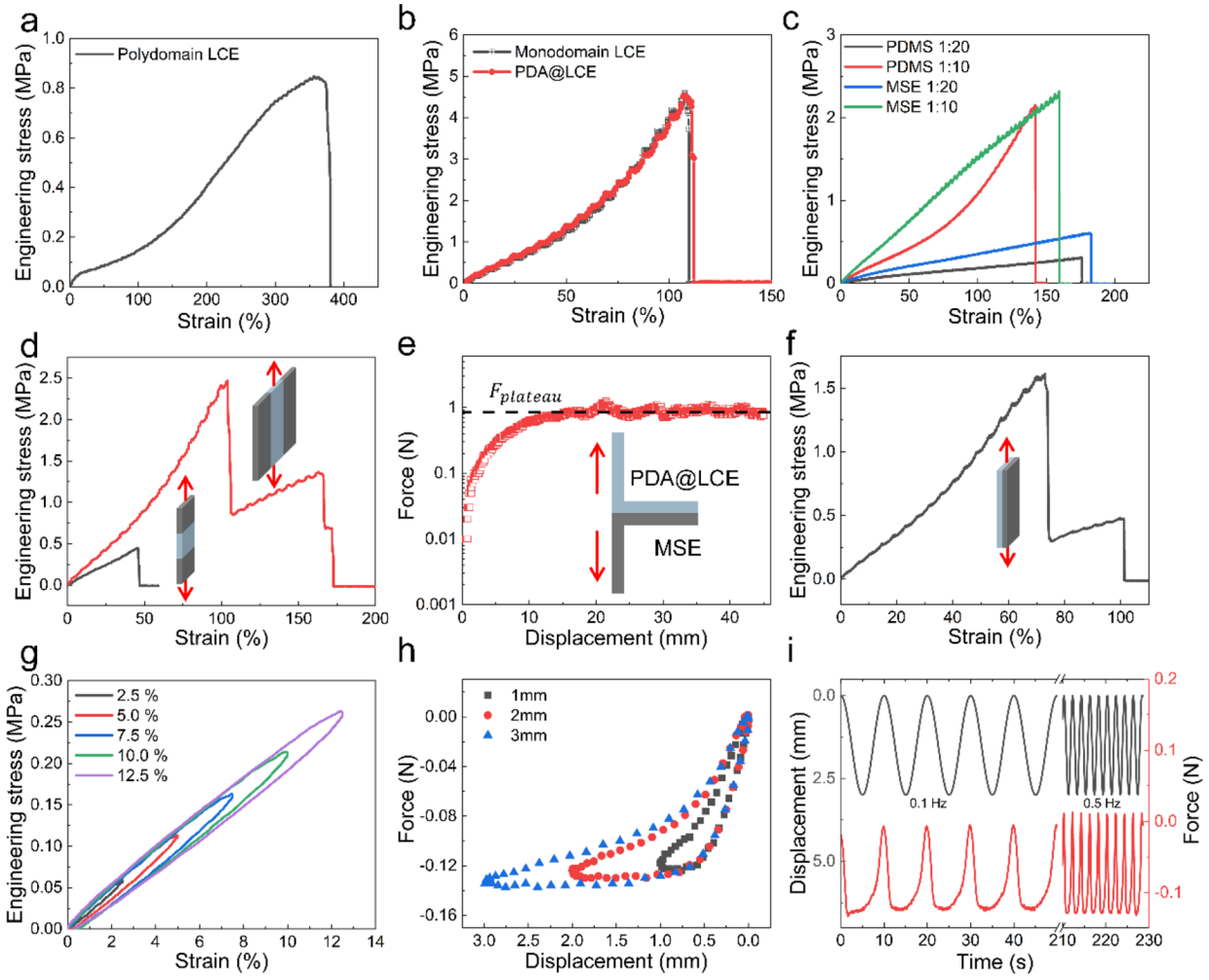

Figure 3. Stress−strain curves of (a) polydomain LCE, (b) monodomain LCE, PDA@LCE, (c) PDMS and MSE. (d) Tensile properties of the in-plane stacking PDA@LCE/MSE along two orthogonal axes. (e) Bonding strength of the PDA@LCE/MSE sample in a 180° peeling test. (f, g) Tensile properties and (h, i) bending properties of the *z* stacking PDA@LCE/MSE sample.

2.9. Finite Element Analysis of PDA@LCE/MSE with Different Configurations. The solid mechanics module in COMSOL is used to calculate the thermal deformation of *z*-like stacking PDA@LCE/MSE samples with different PDA@LCE arrangements and *z* stacking PDA@LCE/MSE samples with different director field directions. Young's modulus and Poisson's ratio of the PDA@LCE are 1.25 MPa and 0.4, respectively. Young's modulus and Poisson's ratio of MSE are 1.5 MPa and 0.4, respectively. When the arrangement of the PDA@LCE or the alignment of the mesogen changes, the thermal expansion coefficient matrix is obtained by decomposing the thermal expansion coefficient according to the arrangement angle or the alignment angle. The ambient temperature is 100 °C. The lower-left corner of the model is clamped. The mesh type is the free tetrahedral mesh.

The solid mechanics and magnetic field modules in COMSOL are used to calculate the magnetodeformation of the sample. A sufficiently large spherical air domain is established and its outer layer is defined as an infinite element domain. The sample is located in the middle of the air domain. The particle chains in MSE are simplified into magnetic strips. The width and orientation angle of the magnetic strip are 0.23 mm and 30°, respectively. According to the width and particle content, the number of magnetic strips is 30. The ambient temperature is room temperature. Young's modulus of PDA@LCE is 4.19 MPa. The permeability of the magnetic strip is 1.3 and that of other parts is 1. The magnitude of the uniform magnetic field is 0.2 T, and its direction is along the thickness of the sample. In the magnetic field module, the force calculation is applied to the magnetic strip part. The magnetic field force is converted into Maxwell stress in the solid mechanics module. The left side of the MSE is constrained. The infinite element domain and the PDA@LCE part are meshed by the sweep method. The mesh of the other parts is the free tetrahedral mesh.

3. RESULTS AND DISCUSSION

3.1. Thermomechanical Properties of LCE and Magnetorheological Properties of MSE. The FTIR spectra of a general polydomain LCE and a polydomain LCE that is further photocured are shown in Figure 2a. A general polydomain LCE is obtained by the Michael addition reaction. Comparing the FTIR spectra of the two polydomain LCEs, the S−H absorption peak at 2571 cm^{-1} shows negligible change, while the C═C absorption peak at 810 cm^{-1} changed significantly. It indicates that the thiol groups are completely converted in the addition reaction and not affected by the photo-polymerization reaction. The acrylate groups remain after the addition reaction, and the remaining part is completely converted in the light-curing reaction. The FTIR spectra reveal the synthesis process in detail. Figure 2b depicts the tensile thermomechanical properties of polydomain LCE. With the increase of temperature, the tensile storage modulus of polydomain LCE shows a trend of first decreasing and then increasing. The loss factor increases first and then decreases.

https://doi.org/10.1021/acsapm.3c00858
ACS Appl. Polym. Mater. 2023, 5, 6199−6211

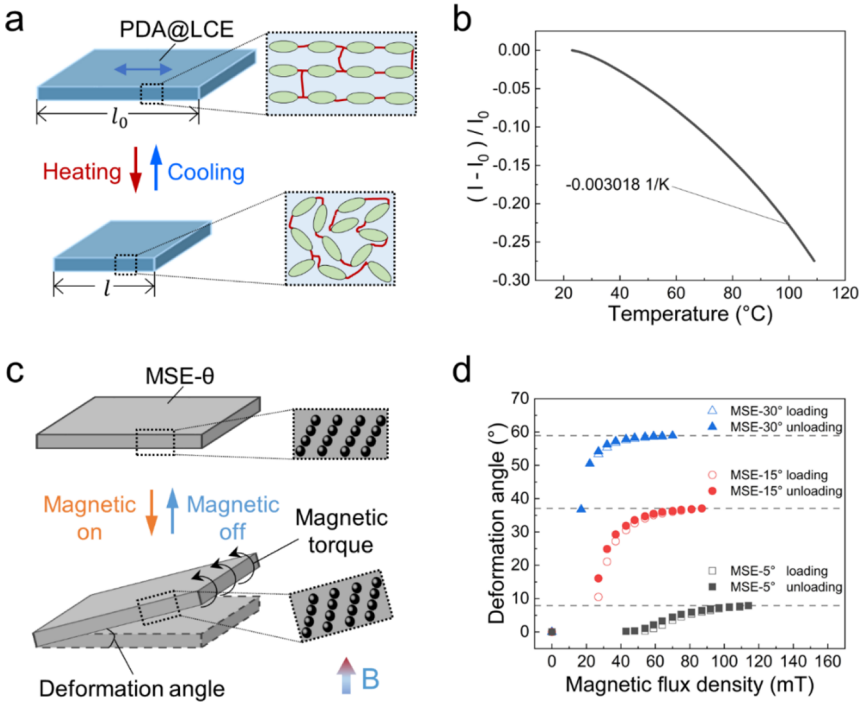

Figure 4. (a) Schematic of thermal deformation of PDA@LCE, where l_0 and l are the original length of LCE and the length after heating, respectively. (b) Effect of temperature on the thermal deformation of PDA@LCE. (c) Schematic of the magnetodeformation of MSE. (d) Deformation angle of the MSE under a uniform magnetic field as a function of magnetic flux density.

The temperature at the peak of the tan δ curve is the glass transition temperature (T_g). The T_g of polydomain LCE is 13 °C. When the temperature is greater than the T_g, there is a plateau in the tan δ curve of polydomain LCE. The appearance of the plateau is attributed to the rotation of the shape anisotropic mesogens in LCE.[42] Figure S2a,b depict the 2D XRD patterns and azimuthal diffraction profiles for polydomain LCE and monodomain LCE, respectively. Compared with polydomain LCE, the 2D XRD pattern of monodomain LCE shows a pair of arcs, indicating a nematic phase. The arrow denotes the aligning direction. The POM images of monodomain LCE presented in Figure S2c also indicates that it is anisotropic. It can be concluded that at room temperature, mesogens in polydomain LCE exhibit an isotropic distribution, whereas those in monodomain LCE are distributed anisotropically. Figure 2c shows the DSC results for polydomain LCE. The isotropic transition temperature (T_i) of the LCE is 79 °C. When the temperature is higher than T_i, the mesogen alignment will change to isotropic. The above results prove that temperature-sensitive LCEs are successfully prepared.

Figure 2d shows the hysteresis loops of CI and MSE with 50 wt % CI. Both CI and MSE have negligible magnetic hysteresis to allow reversible magnetodeformation. Figure 2e shows the magnetorheological properties of PDMS and MSE prepared from different cross-linking contents. As the magnetic flux density increases, the shear storage modulus of PDMS remains constant, while that of MSE gradually increases and reaches the maximum. Under the zero field, the storage modulus of PDMS 1:20, PDMS 1:10, MSE 1:20, and MSE 1:10 is 0.10, 0.24, 0.16, and 0.26 MPa, respectively. The PDMS elastomer with more curing agents exhibits greater modulus. The magneto-induced shear modulus is defined as the difference between the maximum shear modulus and the initial shear modulus. The magneto-induced shear modulus of MSE 1:20 is higher than that of MSE 1:10. Therefore, the mechanical properties and magnetic field response of PDMS elastomers can be easily regulated by changing the content of the curing agent. Figure 2f shows the oscillating shear temperature sweep results for polydomain LCE and MSE 1:20 samples. The shear storage modulus and loss factor of the polydomain LCE change with temperature, similar to the results of the tensile test shown in Figure 2b. However, the storage modulus and loss factor of MSE do not change with temperature. The results indicate that the mechanical properties of PDMS-based elastomers are not sensitive to temperature and can be used in the study of PDA@LCE/MSE.

3.2. Mechanical Properties and Bonding Strength of PDA@LCE/MSE. Figure 3a exhibits the tensile stress−strain curve of polydomain LCE. In the early stage of strain loading, polydomain LCE shows elastic deformation behavior. With the increase of strain, the stress of polydomain LCE continues increasing, and the overall mechanical response is nonlinear. With the increase of the stretching degree, the mesogens in polydomain LCE are gradually oriented in the stretching direction, resulting in the increase of stress. Young's modulus and fracture strain of polydomain LCE are 0.15 MPa and 375%, respectively. The stress−strain curves of monodomain LCE and PDA@LCE are shown in Figure 3b. Young's modulus and fracture strain of monodomain LCE are 4.19 MPa and 108%, respectively. The tensile parameters of PDA@LCE are similar to those of monodomain LCE. Therefore, the mechanical properties of LCE are not changed after coating PDA. The stress−strain curves of PDMS elastomers are shown in Figure 3c. Young's modulus for PDMS 1:20, PDMS 1:10, MSE 1:20, and MSE 1:10 are 0.18, 1.09, 0.35, and 1.50 MPa, respectively. The addition of magnetic particles and the increase in cross-linker content increase the modulus of the PDMS elastomer, which is consistent with the conclusions

https://doi.org/10.1021/acsapm.3c00858
ACS Appl. Polym. Mater. 2023, 5, 6199−6211

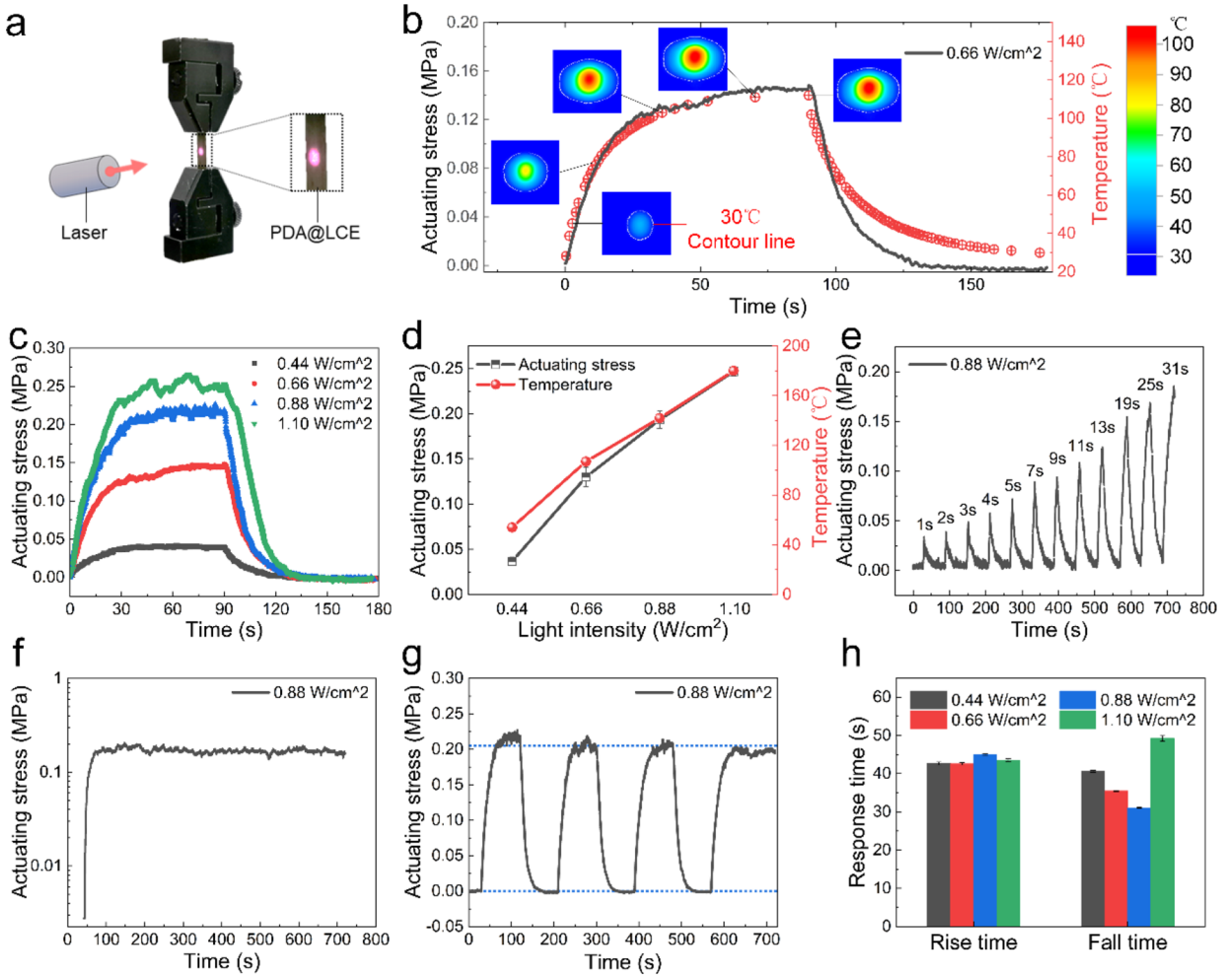

Figure 5. (a) Schematic of the photothermal experiment setup for PDA@LCE. (b) Actuating stress and the maximum temperature of the PDA@LCE sample under the NIR irradiation with an intensity of 0.66 W/cm^2. (c) Change of actuating stress with time under different light intensities. (d) Maximum actuating stress and temperature of the PDA@LCE at different light intensities. Under the laser with light intensity of 0.88 W/cm^2, the effects of (e) irradiation duration, (f) long-term irradiation, and (g) cyclic irradiation on the actuating stress. (h) Response time of actuating stress of PDA@LCE under different light intensities.

obtained from Figure 2e. Compared to PDA@LCE, the MSE has lower Young's modulus and greater fracture strain (Figure 3b,c). Unless otherwise specified, MSE and PDMS with a cross-link ratio of 1:10 are used in subsequent experiments.

The tensile properties of in-plane stacking PDA@LCE/MSE are characterized (Figure 3d). The tensile test along the stack direction is performed with sample with dimensions of 31 mm × 3 mm × 0.4 mm. The modulus and fracture strain of the sample are 0.98 MPa and 46%, respectively. The fracture occurs at the junction of PDA@LCE and MSEs. When a sample with dimensions of 10 mm × 10.5 mm × 0.34 mm is stretched perpendicular to the stacking direction, the tensile modulus is 2.40 MPa. The fracture strains are 105, 166, and 172%, respectively. The primary fracture occurs on PDA@LCE, and secondary and tertiary fracture occurs on the MSEs. The results reveal that the in-plane stacking PDA@LCE/MSE has anisotropic mechanical properties.

A 180° peel experiment is performed on the PDA@LCE/MSE sample with a width of 7 mm and thickness of 1.65 mm. The thickness of PDA@LCE and MSE in the PDA@LCE/MSE is 1.1 and 0.55 mm, respectively. The platform value of the interface bonding force for the PDA@LCE/MSE is 0.9 N (Figure 3e). The interface bonding strength is equal to twice the ratio of the interface bonding force to the width of the sample.[38,43] Therefore, the interface bonding strength of the PDA@LCE/MSE is 257 J/m^2. Figure 3f–g shows the tensile results of a z stacking PDA@LCE/MSE sample (10 mm × 3 mm × 0.7 mm). Young's modulus of the sample is 2.04 MPa. The fracture strains are 74 and 101%, corresponding to the fractures of PDA@LCE and MSE (Figure 3f). Figure 3g depicts that the sample has a small area of hysteresis loop under loading and unloading with strain amplitudes of 2.5, 5, 7.5, 10, and 12.5%. It indicates that the z stacking PDA@LCE/MSE sample has good elasticity at low strain. The bending experiments at a frequency of 1 Hz are also conducted on the sample. The position of the lower chuck of DMA is fixed. The sample is bent and recovered by controlling the movement of the upper chuck. The displacement amplitudes of the upper chuck are 1, 2, and 3 mm, respectively. During the bending process, the force of the sample first increases and then stabilizes; during recovery, the force gradually decreases to the initial value (Figure 3h). When the position of the chuck is the same, the force during bending is greater than that during recovery. It can be attributed to the elasticity of the sample resisting its bending but facilitating its recovery. The larger the amplitude of the chuck displacement, the more parts of the

https://doi.org/10.1021/acsapm.3c00858
ACS Appl. Polym. Mater. 2023, 5, 6199−6211

sample are bent, and thus the greater the force. Figure 3i shows the experimental results of bending at different frequencies. From 0.1 to 0.5 Hz, force over time is not affected by frequency, indicating that the z stacking PDA@LCE/MSE sample can withstand bending at different frequencies.

3.3. Thermal Deformation of PDA@LCE and Magnetodeformation of MSE. Figure 4a shows the schematic of the thermal deformation of PDA@LCE. When the temperature increases, the mesogens in the PDA@LCE gradually change from an anisotropic arrangement to an isotropic arrangement, which causes the PDA@LCE to shrink along the director field direction and to elongate perpendicular to the director field direction. Moreover, the process is reversible (Video S1). Figure 4b shows the ratio of the shrinkage of the PDA@LCE to its original length as a function of temperature. As the temperature increases, the ratio gradually increases, indicating that the amplitude of thermal deformation increases. When the temperature is greater than T_i of the LCE, the ratio increases at a larger rate, which indicates that the PDA@LCE has a large deformation magnitude in an environment with a temperature higher than T_i. Therefore, in subsequent experiments, 100 °C is chosen as the temperature of thermal deformation of the PDA@LCE/MSE. Figure 4b also manifests that the thermal expansion coefficient of the PDA@LCE at 100 °C is 0.003018 1/K. Figure S4 shows the experimental results of the thermal deformation of PDA@LCE. When the PDA@LCE is placed on a hot plate at 100 °C, it gradually shrinks along the director field direction. The sample is then transferred to room temperature to cool. Eventually, the sample returns to its original length, which proves that PDA@LCE has reversible thermal deformability.

Figure 4c depicts the schematic of the magnetodeformation of the MSE. When a magnetic field is applied, the direction of the particle chain tends to the direction of the magnetic field, resulting in the bending deformation of the MSE. When the magnetic field is removed, the MSE returns to its initial state. Figure 4d shows the deformation angle of the MSE-5°, MSE-15°, and MSE-30° under a uniform magnetic field. When the magnetic flux density increases to a certain value, the deformation angle begins to increase. Subsequently, the deformation angle increases with increasing magnetic flux density until the maximum is reached. When the magnetic flux density is higher, the MSE is subjected to greater magnetic bending moment, resulting in a larger deformation angle. When the particle chain orientation of the MSE is close to the direction of the magnetic field, the magnetic potential energy of the MSE is the minimum and the deformation angle reaches the maximum. As the magnetic flux density decreases, the deformation angle gradually returns to zero. When the magnetic flux density increases to 17 mT, the deformation angle of the MSE-30° sample is zero. However, when the magnetic flux density decreases to 17 mT, the deformation angle of the MSE-30° is 36.7°. This is because when the magnetic field is applied, the magnetic bending moment needs to overcome gravity and adhesion. During the unloading of the magnetic field, there is no adhesion. Under the same magnetic flux density, the larger the orientation angle of the particle chain, the greater the deformation angle. This is also due to the greater magnetic bending moment on the MSE with a larger particle chain orientation angle. The influence of the particle chain orientation on the deformation angle has been investigated in our previous studies.[44] Figure S5 shows the deformation angle of the MSE under a nonuniform magnetic field. The experimental results are similar to those in Figure 4d. The above results indicate that the magnetodeformation of MSE can be controlled by particle chain orientation and magnetic flux density.

3.4. Photothermal Response of PDA@LCE. The photothermal actuating stress and response time of PDA@LCE are studied. The experimental setup is shown in Figure 5a. A NIR laser is used to irradiate the middle of the PDA@LCE. Both ends of the PDA@LCE are clamped by the chuck of the DMA. Under the irradiation of the laser, the PDA converts light energy into heat energy, causing the PDA@LCE to shrink. The shrinkage force is recorded. Figure 5b shows the actuating stress and temperature of the PDA@LCE over time under NIR irradiation with a light intensity of 0.66 W/cm^2. As the irradiation time increases, the actuating stress gradually increases and then reaches a maximum value. After the irradiation is removed at 90 s, the actuating stress gradually decreases to zero. The illustrations in Figure 5b manifest the temperature distribution of the sample surface. The temperature in the center of the sample is the highest. The 30 °C contour of the thermal spot is marked with a white line as the outline of the thermal spot, reflecting the size of the thermal spot. As the actuating stress increases, both the highest temperature and area of the thermal spot first becomes larger and then remains unchanged. It indicates that the photothermal actuating stress of the PDA@LCE is related to the surface temperature.

Figure 5c shows the actuating stress over time for PDA@LCE at different light intensities. The maximum values of actuating stress and surface center temperature are summarized in Figure 5d. The maximum actuating stress increases with increasing light intensity, which indicates that the photothermal actuating performance of the PDA@LCE can be adjusted by irradiation intensity. The increase rate is the largest at the irradiation intensity of 0.66 W/cm^2. When the light intensity is 0.66 W/cm^2, the maximum temperature on the PDA@LCE is 107 °C, which is higher than the T_i. At this temperature, the deformation rate of the PDA@LCE increases more (Figure 4b), but its modulus is lower (Figure 2b). The temperature affects deformation more than its effect on modulus. Therefore, the increase rate in the actuating stress of the PDA@LCE increases.

Under the irradiation intensity of 0.88 W/cm^2, the effect of irradiation duration on the actuating stress is explored (Figure 5e). When the irradiation duration increases from 1 to 31 s, the actuating stress of PDA@LCE increases from 0.034 to 0.185 MPa. Therefore, the transient actuating stress of PDA@LCE can be adjusted by irradiation time. Figure 5f depicts the actuating stress of PDA@LCE irradiated continuously for 680 s. After turning on the laser at 40 s, the actuating stress first increases to the maximum value and then remains stable, which indicates that the photothermal actuation performance of PDA@LCE has good stability. The PDA@LCE is subjected to alternating laser irradiation tests (Figure 5g). The initial and maximum actuating stresses are kept 0 and 0.205 MPa, respectively, revealing the reversible actuation capability of PDA@LCE. Figure 5h summarizes the response time for actuating stress to reach the maximum value (rise time) and recover to the initial value (fall time). The rise time and fall time of PDA@LCE are approximately 43 and 39 s, respectively, which is a reasonable photothermal actuation response time. The response time of PDA@LCE could be reduced by changing the visco-elasticity of the matrix,

https://doi.org/10.1021/acsapm.3c00858
ACS Appl. Polym. Mater. 2023, 5, 6199−6211

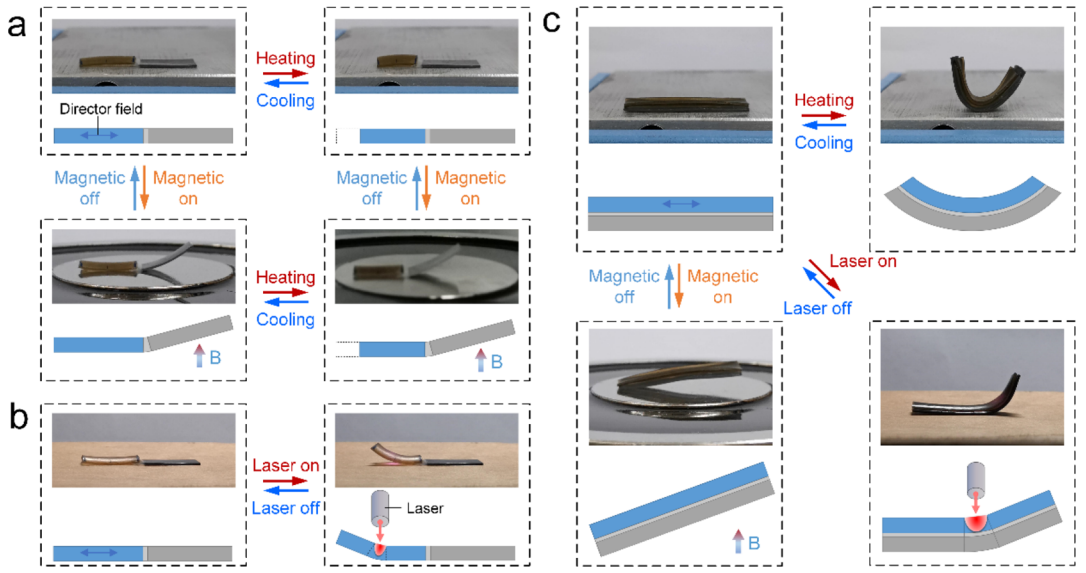

Figure 6. (a) Thermal deformation, magnetodeformation, and (b) photodeformation of in-plane stacking PDA@LCE/MSE. (c) Deformation and recovery of the *z* stacking PDA@LCE/MSE under different stimuli.

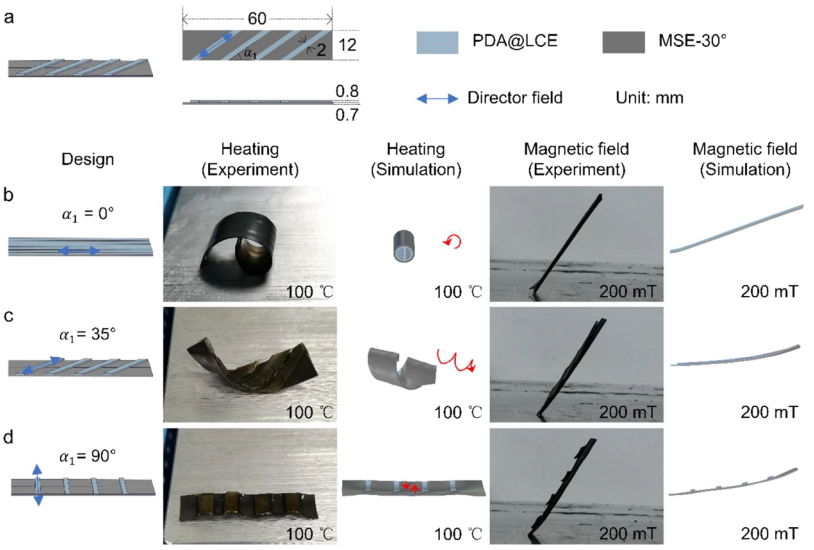

Figure 7. (a) Geometric dimensions of the *z*-like stacking PDA@LCE/MSE composed of PDA@LCE strips and MSE baseplate. Thermally and magnetically induced 3D deformations of different *z*-like stacking PDA@LCE/MSE samples with α_1 of (b) 0°, (c) 35°, and (d) 90°, respectively.

increasing the energy conversion efficiency of the PDA and increasing the size of the infrared spot. Therefore, the adjustable, reversible, stable, and fast photothermal actuation performance of PDA@LCE enables PDA@LCE/MSE to have ideal photothermal deformation capability.

3.5. Deformation Mechanism of PDA@LCE/MSE. Based on the good interface strength and stimulus response performance of PDA@LCE and MSE, in-plane stacking PDA@LCE/MSE and *z* stacking PDA@LCE/MSE are developed, respectively. Figure 6 and Videos S2, S3, and S4 show the deformation of the sample. Figure 6a demonstrates the thermally induced and magnetically induced deformation of the in-plane stacking PDA@LCE/MSE. When the temperature increases or decreases, the PDA@LCE part on the PDA@LCE/MSE shrinks or recovers. When the magnetic field is applied or removed, the MSE part bends or recovers, while the PDA@LCE part is not affected. When the thermal and magnetic fields are applied simultaneously, the two parts of the PDA@LCE/MSE independently exhibit deformation response. Therefore, the in-plane stacking PDA@LCE/MSE has four configurations under the control of thermal and magnetic field. When the laser irradiates the PDA@LCE part of the PDA@LCE/MSE, the PDA@LCE part bends around the irradiated position. When the irradiation is removed, the sample returns to its initial configuration (Figure 6b). The PDA increases the temperature of the irradiated position on the PDA@LCE, causing the LCE to shrink. The high temperature is mainly concentrated on the laser-close side of the PDA@LCE. Therefore, one side close to the laser shrinks more than the other positions, resulting in bending deformation of the PDA@LCE part.

Figure 6c shows the deformation of the *z* stacking PDA@LCE/MSE. The *z* stacking PDA@LCE/MSE exhibits bending deformation under both thermal and magnetic fields. Under the magnetic field, the MSE part is subjected to the magnetic bending moment, resulting in off-plane bending deformation of

https://doi.org/10.1021/acsapm.3c00858
ACS Appl. Polym. Mater. 2023, 5, 6199−6211

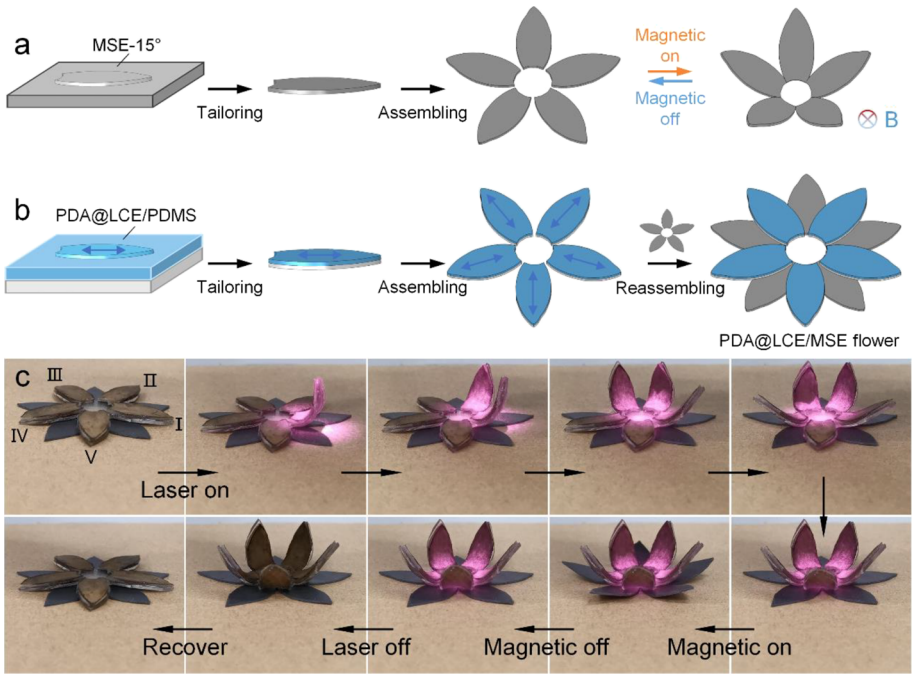

Figure 8. Assembly process of (a) MSE flower and (b) flower-like PDA@LCE/MSE. (c) Multimode deformation of the flower-like PDA@LCE/MSE under the control of infrared laser and magnetic field.

the sample. When the temperature increases, the PDA@LCE part on the *z* stacking PDA@LCE/MSE sample shrinks and the MSE part acts as a passive material, so the sample exhibits bending deformation. When a laser is applied, the temperature of the PDA@LCE at the irradiated location increases, causing the sample to bend. Owing to the reversible stimulus response of PDA@LCE and MSE, the deformation response of *z* stacking PDA@LCE/MSE to temperature, magnetic field, and laser is reversible. To further analyze the thermal deformation of the *z* stacking PDA@LCE/MSE sample, finite element calculations are performed. The influence of the modulus ratio and thickness ratio on the thermal deformation is explored by changing the thickness and modulus of the MSE. The results and analysis are presented in Section S2 of the Supporting Information.

3.6. Complex Shape-Deformations of PDA@LCE/MSE.

The traditional magnetically sensitive composites only show bending deformation. The thermal-induced shape-morphing of the LCE is the simple shrinkage deformation. Here, through structural design, the PDA@LCE/MSE can achieve sophisticated 3D deformations. Figure 7 showcases the deformation response of several *z*-like stacking PDA@LCE/MSE under thermal and magnetic fields. The PDA@LCE strips are assembled on the MSE-30° baseplate (Figure 7a). The angle between the longitudinal direction of the PDA@LCE strip and that of the MSE baseplate is α_1. The direction of the arrow represents the director field direction of the PDA@LCE strip. The director field direction is along its longitudinal direction.

The thermally and magnetically induced deformation of samples for α_1 = 0°, α_1 = 35°, and α_1 = 90° is investigated (Figure 7b–d). The deformation results are also obtained by the finite element method. On the hot plate, the sample for α_1 = 0° is rolled like a scroll along the longitudinal direction of the MSE. The sample for α_1 = 35° exhibits a special curling behavior. The sample for α_1 = 90° is bent along the transverse direction of the MSE. The calculation results of the thermal deformation are similar to the experimental results. When the sample is in a high temperature environment, the PDA@LCE strip shrinks along its longitudinal direction, and the MSE baseplate does not respond to the temperature change. This mismatch of deformations causes the sample to bend along the longitudinal direction of the PDA@LCE strip. For samples with α_1 of 0 and 90°, the longitudinal direction of the PDA@LCE strip is parallel and perpendicular to that of the MSE baseplate, respectively. Therefore, the samples for α_1 = 0° and α_1 = 90° are curved along the longitudinal or transverse direction of the MSE baseplate. For the sample with α_1 of 35°, the longitudinal direction of the PDA@LCE strip is at an angle with the geometric principal axis direction of the MSE baseplate, causing the sample to curl into the helical shape.

The magnetodeformation results of *z*-like stacking PDA@LCE/MSE show that all samples are bent under a uniform magnetic field. When the external magnetic field is applied, the magnetic bending moment on the MSE-30° part causes the sample to bend. The experimental results manifest that the magnetodeformation angle of the three samples is the same. The calculation results show that the deformation amplitude of the three samples is different. The difference between the experimental results and the calculation results is caused by the different grid distribution in the computational model. The above results indicate that the *z*-like stacking PDA@LCE/MSE sample has the ability of complex 3D deformation.

The influence of the mesogen alignment on the deformation of PDA@LCE/MSE is investigated. Figure S12a shows a *z* stacking PDA@LCE/MSE sample consisting of PDA@LCE plate and MSE-30° plate with the same length and width. The angle between the director field direction of the PDA@LCE plate and its longitudinal direction is β_1. Figure S12b–d manifests the deformation results of *z* stacking PDA@LCE/MSE samples with β_1 of 0, 48, and 90°, respectively. With the increase of β_1, the sample exhibits the deformation morphology of roll, curl, and bend, respectively, which is

https://doi.org/10.1021/acsapm.3c00858
ACS Appl. Polym. Mater. 2023, 5, 6199–6211

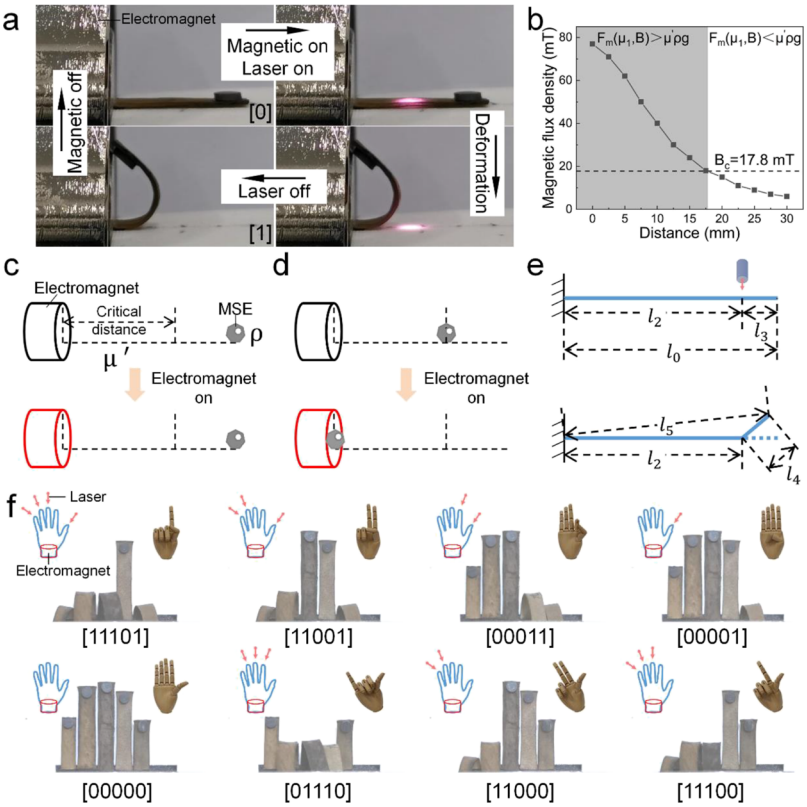

Figure 9. (a) Deformation and recovery of the thermally triggered magnetic holding actuator made of PDA@LCE/MSE. (b) Change of the magnetic flux density of the electromagnet with distance. (c, d) Magnetic actuation of the electromagnet on distant MSE. (e) Schematic of the thermally triggered magnetic holding actuator. (f) Different gestures displayed by a handlike actuator consisting of the PDA@LCE/MSE array.

similar to the results in Figure 7b–d. The results of magnetodeformation reveal that the three *z* stacking PDA@LCE/MSE samples have the same magneto-induced bending deformation. Therefore, by changing the distribution of PDA@LCE or the alignment of mesogens, PDA@LCE/MSE shows different complex deformation morphologies, which exhibits application potential in the packaging and transportation of items.

3.7. Multimode Morphing of Flower-like PDA@LCE/MSE. To demonstrate the multimode deformation capability of the PDA@LCE/MSE, a flower-like PDA@LCE/MSE is assembled using MSE-15° and PDA@LCE/PDMS. As shown in Figure 8a, MSE is cut into the shape of petal with scissors, and five MSE petals are arranged on a silicon wafer in the shape of the flower. The gap in the center of the flower is filled with the PDMS mixture. After 5 h of heating at 50 °C, the vulcanization of PDMS allows MSE petals to assemble into flowers. To prepare PDA@LCE/PDMS flower, the PDA@LCE plate and PDMS plate are first combined using the method of preparing *z* stacking PDA@LCE/MSE. According to the director field direction of the PDA@LCE petal along its longitudinal direction, PDA@LCE/PDMS is cut into the shape of the petal with scissors. Similarly, five PDA@LCE/PDMS petals are arranged on the silicon wafer in the shape of the flower and the center of the flower is filled with the PDMS mixture. Through curing PDMS, the PDA@LCE/PDMS flower is obtained. Finally, the flower-like PDA@LCE/MSE is manufactured by coating the PDMS mixture in the center of the MSE flower and assembling it with the PDA@LCE/PDMS flower (Figure 8b).

Figure 8c and Video S5 demonstrate the deformation of the flower-like PDA@LCE/MSE under infrared light and magnetic field. The sample is placed on the surface of an electromagnet. The infrared light is located above the sample. When the PDA@LCE/PDMS petal I is irradiated by the light, it shows bending deformation, and the other petals do not respond. Subsequently, the light is moved to simultaneously irradiate PDA@LCE/PDMS petal I and petal II. Petal II also exhibits a curved configuration. Then, the irradiation range of the infrared light is extended to petal III, petal IV, and petal V. All the PDA@LCE/PDMS petals are gradually deformed. A magnetic field is then applied to the sample using the electromagnet. All the MSE-15° petals on the sample simultaneously show an off-plane bending deformation. When the magnetic field is removed, the deformation of MSE-15° petals is restored. Finally, with the infrared light turned off, all the PDA@LCE/PDMS petals gradually return to their initial configuration. This process indicates that the responsiveness of flower-like PDA@LCE/MSE to infrared light gives it the ability to deform locally and actuate sequentially. Compared with the global deformation response of traditional LCE and MSE, the deformation mode of PDA@LCE/MSE is greatly increased.

3.8. Applications of PDA@LCE/MSE for Logic Gesture. The response of PDA@LCE/MSE to temperature, magnetic field, and light is reversible. When the stimulus is removed, the deformation is restored, which has an adverse effect on deformation control. For example, when only petal I and petal III are bent, two infrared light should be employed to control petal I and petal III, respectively. Here, a PDA@LCE/MSE-based thermally triggered magnetic holding actuator with

https://doi.org/10.1021/acsapm.3c00858
ACS Appl. Polym. Mater. 2023, 5, 6199−6211

excellent deformation control is designed. As shown in Figure 9a, the actuator is obtained by gluing the MSE block to one end of the PDA@LCE strip with PDMS. The other end of the PDA@LCE strip is close to the surface of the electromagnet (XDA-50/42). The director field direction of the PDA@LCE follows its longitudinal direction. When the electromagnet is turned on, the actuator does not show deformation response due to the distance of the MSE block from the electromagnet. After applying an infrared laser, the PDA@LCE strip bends, which causes the MSE block to approach the electromagnet and suffer from an increased magnetic actuation. Eventually, the MSE block is attracted to the electromagnet surface, and the actuator exhibits bending deformation. With the infrared laser removed, the deformation of the actuator can be preserved. When the electromagnet is turned off, the magnetic force on the MSE block disappears. Due to the good elasticity of the PDA@LCE strips, the actuator returns to its initial configuration. The thermally triggered magnetic holding actuator can maintain the deformation configuration after the infrared laser is removed, showing good deformation control ability.

Figure 9b manifests the magnetic flux density of the electromagnet. The farther away from the electromagnet, the smaller the magnetic flux density. After the electromagnet is activated, the MSE far away from the electromagnet stays in place due to the weak magnetic force (Figure 9c). When the distance between the MSE and the electromagnet is reduced to the critical distance corresponding to the critical magnetic field B_c, the magnetic force overcomes the frictional force and the MSE is instantly attracted (Figure 9d). The magnitude of the B_c depends only on the magnetic permeability and density of the MSE. The MSE block used in the actuator is MSE with a magnetic particle content of 50 wt %. The magnitude of the B_c of the MSE is 17.8 mT. Therefore, the critical distance for the electromagnet is 17.8 mm. The schematic of the thermally triggered magnetic holding actuator is shown in Figure 9e. The size of the MSE is much smaller than PDA@LCE, so the distance from the MSE to the electromagnet is approximately equal to the initial length of the PDA@LCE strip l_0. When irradiated by laser, the PDA@LCE will bend, which causes the distance to become l_5, less than the sum of l_2 and l_4. It can be seen that the l_4 is not greater than l_3. Ultimately, l_5 is always less than l_0. The design criterion is that the critical distance is between the l_0 and the l_5. Initially, the l_0 is greater than the critical distance, and the MSE is not attracted. After turning on the laser, the l_5 is less than the critical distance, triggering the MSE to be attracted.

A hand-like actuator is constructed using five PDA@LCE/MSE thermally triggered magnetic holding actuators (Figure 9f). Each PDA@LCE/MSE actuator has two configurations: an initial configuration (represented by "0" state) and a curved configuration (represented by "1" state) (Figure 9a). After being irradiated by laser, the PDA@LCE/MSE changes from the "0" state to the "1" state. After removing the magnetic field, the PDA@LCE/MSE returns to the "0" state. Therefore, the handlike actuator has 2^5 encoding states. Figure 9f and Videos S6 and S7 exhibit the configuration and encoding status of the hand-like actuator representing the numbers 1 through 8, respectively. The (0,0,0,0,0) code status represents that the five PDA@LCE/MSE are all initial, and the configuration of the hand-like actuator is similar to the gesture for the number 5. Using an infrared laser to bend the fourth and fifth PDA@LCE/MSE, the encoding status of the handlike actuator becomes (0,0,0,1,1). In this case, its configuration can represent the number 3. After removing the magnetic field, the coding status of the handlike actuator returns to (0,0,0,0,0) and can be encoded again. Moreover, the response time of each thermally triggered magnetic holding actuator is about 4 s. Therefore, PDA@LCE/MSE thermally triggered magnetic holding actuator has controllable, reversible, and programmable deformation capabilities, providing a paradigm for flexible logic circuits.

4. CONCLUSIONS

In summary, we report a multi-stimuli responsive PDA@LCE/MSE actuator with multimode and controllable complex shape-deformations ground on reliable mechanical bonding strength and photothermal conversion ability. Through varying the stacking modes of PDA@LCE/MSE or the director field of LCE, the actuators exhibit a variety of sophisticated deformations including twisting, rolling, bending, contracting, and their combinations under simple control. The deformation amplitude can be precisely regulated by modulating the strength of the external stimuli, the particle chain orientation of the MSE, and the modulus ratio and the thickness ratio of the components. Moreover, due to the introduction of photothermal PDA, the LCE contracts at the location where the light is concentrated, resulting in local and sequential actuation capabilities of the actuator, which addresses the intrinsic limitation of magnetic and thermal responsive actuators. Controlled by magnetic field and lasers, the flower-like PDA@LCE/MSE actuator has various deformation modes and simulates the blooming process of flowers. Furthermore, the thermally triggered magnetic holding actuator based on PDA@LCE/MSE has excellent controllability, reversibility, and programmability and is designed as a logic actuator that can display gesture variations. Therefore, combining PDA@LCE with MSE is a facile and effective strategy to obtain multi-stimuli responsive actuators with multimode programmable deformation, which benefits multifunctional applications including biomedicine, morphological computing, and flexible electronics.

■ ASSOCIATED CONTENT

Supporting Information

The Supporting Information is available free of charge at https://pubs.acs.org/doi/10.1021/acsapm.3c00858.

Photographs of polydomain LCE; monodomain LCE and PDA@LCE at room temperature; 2D XRD patterns; azimuthal intensity scan; POM images of polydomain LCE and monodomain LCE; tensile stress−strain curve for LCE at 100 °C; experimental results of thermal deformation of PDA@LCE; change of the deformation angle with magnetic flux density under nonuniform magnetic field; curvature nephogram of the PDA@LCE/MSE samples with different modulus ratios; curvature nephogram of the lower surface of the MSE and the curvature value of the center point at different modulus ratios; σ_{xx} stress nephogram on the sides of the PDA@LCE and MSE at different modulus ratios; curvature nephogram of the PDA@LCE/MSE samples with different thickness ratios; curvature nephogram of the lower surface of the MSE and the curvature value of the center point at different thickness ratios; σ_{xx} stress nephogram on the sides of the PDA@LCE and MSE at

https://doi.org/10.1021/acsapm.3c00858
ACS Appl. Polym. Mater. 2023, 5, 6199−6211

different thickness ratios; and *z* stacking PDA@LCE/MSE consisting of PDA@LCE strips with different mesogen alignments and MSE baseplate (PDF)

Thermal deformation and recovery of the PDA@LCE (MP4)

Thermal deformation of in-plane stacking PDA@LCE/MSE sample and *z* stacking PDA@LCE/MSE sample (MP4)

Magnetodeformation and recovery of the PDA@LCE/MSE sample (MP4)

Photodeformation of and recovery of the PDA@LCE/MSE sample (MP4)

Various deformations of the flower-like actuator under infrared light at different positions (MP4)

Different gestures exhibited by a hand-like actuator under the control of a laser and magnetic field (MP4)

Different gestures exhibited by a hand-like actuator under the control of a laser and magnetic field (MP4)

AUTHOR INFORMATION

Corresponding Authors

Yu Wang − *CAS Key Laboratory of Mechanical Behavior and Design of Materials, Department of Modern Mechanics, University of Science and Technology of China, 230027 Hefei, China*; Email: wyu@ustc.edu.cn

Xinglong Gong − *CAS Key Laboratory of Mechanical Behavior and Design of Materials, Department of Modern Mechanics, University of Science and Technology of China, 230027 Hefei, China*; orcid.org/0000-0001-6997-9526; Email: gongxl@ustc.edu.cn

Authors

Jingyi Zhang − *CAS Key Laboratory of Mechanical Behavior and Design of Materials, Department of Modern Mechanics, University of Science and Technology of China, 230027 Hefei, China*

Yuxi Sun − *CAS Key Laboratory of Mechanical Behavior and Design of Materials, Department of Modern Mechanics, University of Science and Technology of China, 230027 Hefei, China*

Shuaishuai Sun − *CAS Key Laboratory of Mechanical Behavior and Design of Materials, Department of Precision Machinery and Instrumentation, University of Science and Technology of China, 230027 Hefei, China*

Zhenbang Xu − *CAS Key Laboratory of On-Orbit Manufacturing and Integration for Space, Optics System, Changchun Institute of Optics, Fine Mechanics and Physics, Chinese Academy of Sciences, 130033 Changchun, China*

Jun Li − *Anhui Weiwei Rubber Parts Group Co. Ltd., 231460 Tongcheng, China*

Ji Li − *Anhui Weiwei Rubber Parts Group Co. Ltd., 231460 Tongcheng, China*

Complete contact information is available at: https://pubs.acs.org/10.1021/acsapm.3c00858

Notes

The authors declare no competing financial interest.

ACKNOWLEDGMENTS

Authors X.G., J.Z., Y.W., Y.S., S.S., Z.X., J.L. and J.L. received funding from the National Natural Science Foundation of China (Grant No. 11972337, 11972343, 12132016) and the Anhui's Key R&D Program of China (202104a05020009). Thanks to the instrumentation support from engineering practice center of USTC.

ABBREVIATIONS

FTIR, fourier transform infrared; XRD, x-ray diffraction; POM, polarized optical microscope; NIR, near-infrared; DoF, degree of freedom; MSE, magnetically sensitive elastomer; LCE, liquid crystal elastomer; PDA, polydopamine; CI, carbonyl iron; PDMS, poly(dimethylsiloxane); DSC, differential scanning calorimetry; T_i, isotropic transition temperature; T_g, glass transition temperature

REFERENCES

(1) Wani, O. M.; Verpaalen, R.; Zeng, H.; Priimagi, A.; Schenning, A. An Artificial Nocturnal Flower Via Humidity-Gated Photoactuation in Liquid Crystal Networks. *Adv. Mater.* **2019**, *31*, No. e1805985.

(2) Ma, B.; Xu, C.; Cui, L.; Zhao, C.; Liu, H. Magnetic Printing of Liquid Metal for Perceptive Soft Actuators with Embodied Intelligence. *ACS Appl. Mater. Interfaces* **2021**, *13*, 5574−5582.

(3) Zhao, Z.; Wu, J.; Mu, X.; Chen, H.; Qi, H. J.; Fang, D. Origami by Frontal Photopolymerization. *Sci. Adv.* **2017**, *3*, No. e1602326.

(4) Erb, R. M.; Sander, J. S.; Grisch, R.; Studart, A. R. Self-Shaping Composites with Programmable Bioinspired Microstructures. *Nat. Commun.* **2013**, *4*, 1712.

(5) Zhang, X.; Wu, Y.; Li, Y.; Jiang, H.; Yang, Q.; Wang, Z.; Liu, J.; Wang, Y.; Fan, X.; Kong, J. Small-Scale Soft Grippers with Environmentally Responsive Logic Gates. *Mater. Horiz.* **2022**, *9*, 1431−1439.

(6) Shintake, J.; Rosset, S.; Schubert, B.; Floreano, D.; Shea, H. Versatile Soft Grippers with Intrinsic Electroadhesion Based on Multifunctional Polymer Actuators. *Adv. Mater.* **2016**, *28*, 231−238.

(7) Kim, J.; Chung, S. E.; Choi, S. E.; Lee, H.; Kim, J.; Kwon, S. Programming Magnetic Anisotropy in Polymeric Microactuators. *Nat. Mater.* **2011**, *10*, 747−752.

(8) Ren, Z.; Hu, W.; Dong, X.; Sitti, M. Multi-Functional Soft-Bodied Jellyfish-Like Swimming. *Nat. Commun.* **2019**, *10*, 2703.

(9) Novelino, L. S.; Ze, Q.; Wu, S.; Paulino, G. H.; Zhao, R. Untethered Control of Functional Origami Microrobots with Distributed Actuation. *Proc. Natl. Acad. Sci. U. S. A.* **2020**, *117*, 24096−24101.

(10) Li, C.; Jiao, Y.; Lv, X.; Wu, S.; Chen, C.; Zhang, Y.; Li, J.; Hu, Y.; Wu, D.; Chu, J. In Situ Reversible Tuning from Pinned to Roll-Down Superhydrophobic States on a Thermal-Responsive Shape Memory Polymer by a Silver Nanowire Film. *ACS Appl. Mater. Interfaces* **2020**, *12*, 13464−13472.

(11) Wu, J.; Yao, S.; Zhang, H.; Man, W.; Bai, Z.; Zhang, F.; Wang, X.; Fang, D.; Zhang, Y. Liquid Crystal Elastomer Metamaterials with Giant Biaxial Thermal Shrinkage for Enhancing Skin Regeneration. *Adv. Mater.* **2021**, *33*, No. 2106175.

(12) Wang, X.; Lin, D.; Zhou, Y.; Jiao, N.; Tung, S.; Liu, L. Multistimuli-Responsive Hydroplaning Superhydrophobic Microrobots with Programmable Motion and Multifunctional Applications. *ACS Nano* **2022**, *16*, 14895−14906.

(13) Liu, J. A.; Gillen, J. H.; Mishra, S. R.; Evans, B. A.; Tracy, J. B. Photothermally and Magnetically Controlled Reconfiguration of Polymer Composites for Soft Robotics. *Sci. Adv.* **2019**, *5*, No. eaaw2897.

(14) Weng, M. C.; Tang, Z. D.; Zhu, J. M. Multi-Responsive Soft Paper-Based Actuators with Programmable Shape-Deformations. *Sens. Actuators A Phys.* **2021**, *331*, No. 113016.

(15) Du, X. M.; Cui, H. Q.; Xu, T. T.; Huang, C. Y.; Wang, Y. L.; Zhao, Q. L.; Xu, Y. S.; Wu, X. Y. Reconfiguration, Camouflage, and Color-Shifting for Bioinspired Adaptive Hydrogel-Based Millirobots. *Adv. Funct. Mater.* **2020**, *30*, No. 1909202.

(16) Ma, C.; Wu, S.; Ze, Q.; Kuang, X.; Zhang, R.; Qi, H. J.; Zhao, R. Magnetic Multimaterial Printing for Multimodal Shape Transformation with Tunable Properties and Shiftable Mechanical Behaviors. *ACS Appl. Mater. Interfaces* **2021**, *13*, 12639−12648.
(17) Zhu, H.; Wang, Y.; Ge, Y.; Zhao, Y.; Jiang, C. Kirigami-Inspired Programmable Soft Magnetoresponsive Actuators with Versatile Morphing Modes. *Adv. Sci.* **2022**, *9*, No. e2203711.
(18) Jiralerspong, T.; Bae, G.; Lee, J. H.; Kim, S. K. Wireless Control of Two- and Three-Dimensional Actuations of Kirigami Patterns Composed of Magnetic-Particles-Polymer Composites. *ACS Nano* **2020**, *14*, 17589−17596.
(19) Yang, Y. F.; Li, M. Y.; Xu, F. A 3d Hard-Magnetic Rod Model Based on Co-Rotational Formulations. *Acta Mech. Sin.* **2022**, *38*, 222085.
(20) Zhang, J.; Diller, E. Untethered Miniature Soft Robots: Modeling and Design of a Millimeter-Scale Swimming Magnetic Sheet. *Soft Robot.* **2018**, *5*, 761−776.
(21) Schmauch, M. M.; Mishra, S. R.; Evans, B. A.; Velev, O. D.; Tracy, J. B. Chained Iron Microparticles for Directionally Controlled Actuation of Soft Robots. *ACS Appl. Mater. Interfaces* **2017**, *9*, 11895−11901.
(22) Qi, S.; Fu, J.; Xie, Y. P.; Li, Y. P.; Gan, R. Y.; Yu, M. Versatile Magnetorheological Plastomer with 3d Printability, Switchable Mechanics, Shape Memory, and Self-Healing Capacity. *Compos. Sci. Technol.* **2019**, *183*, No. 107817.
(23) Testa, P.; Style, R. W.; Cui, J.; Donnelly, C.; Borisova, E.; Derlet, P. M.; Dufresne, E. R.; Heyderman, L. J. Magnetically Addressable Shape-Memory and Stiffening in a Composite Elastomer. *Adv. Mater.* **2019**, *31*, No. e1900561.
(24) Tang, J. D.; Sun, B. A. Reprogrammable Shape Transformation of Magnetic Soft Robots Enabled by Magnetothermal Effect. *Appl. Phys. Lett.* **2022**, *120*, 244101.
(25) Kuang, X.; Wu, S.; Ze, Q.; Yue, L.; Jin, Y.; Montgomery, S. M.; Yang, F.; Qi, H. J.; Zhao, R. Magnetic Dynamic Polymers for Modular Assembling and Reconfigurable Morphing Architectures. *Adv. Mater.* **2021**, *33*, No. 2102113.
(26) Deng, H.; Sattari, K.; Xie, Y.; Liao, P.; Yan, Z.; Lin, J. Laser Reprogramming Magnetic Anisotropy in Soft Composites for Reconfigurable 3d Shaping. *Nat. Commun.* **2020**, *11*, 6325.
(27) Tang, D. F.; Zhang, C. Q.; Sun, H. N.; Dai, H. Z.; Xie, J.; Fu, J. Z.; Zhao, P. Origami-Inspired Magnetic-Driven Soft Actuators with Programmable Designs and Multiple Applications. *Nano Energy* **2021**, *89*, No. 106424.
(28) Eshaghi, M.; Ghasemi, M.; Khorshidi, K. Design, Manufacturing and Applications of Small-Scale Magnetic Soft Robots. *Extreme Mech. Lett.* **2021**, *44*, No. 101268.
(29) Roach, D. J.; Sun, X. H.; Peng, X. R.; Demoly, F.; Zhou, K.; Qi, H. J. 4d Printed Multifunctional Composites with Cooling-Rate Mediated Tunable Shape Morphing. *Adv. Funct. Mater.* **2022**, *32*, No. 2203236.
(30) Chen, J.; Johnson, A. S.; Weber, J.; Akomolafe, O. I.; Jiang, J. H.; Peng, C. H. Programmable Light-Driven Liquid Crystal Elastomer Kirigami with Controlled Molecular Orientations. *Adv. Intell. Syst.* **2022**, *4*, No. 2100233.
(31) Zhao, T. H.; Zhang, Y. L.; Fan, Y. Y.; Wang, J.; Jiang, H. Q.; Lv, J. A. Light-Modulated Liquid Crystal Elastomer Actuator with Multimodal Shape Morphing and Multifunction. *J. Mater. Chem. C* **2022**, *10*, 3796−3803.
(32) Tabrizi, M.; Ware, T. H.; Shankar, M. R. Voxelated Molecular Patterning in Three-Dimensional Freeforms. *ACS Appl. Mater. Interfaces* **2019**, *11*, 28236−28245.
(33) Ambulo, C. P.; Tasmim, S.; Wang, S.; Abdelrahman, M. K.; Zimmern, P. E.; Ware, T. H. Processing Advances in Liquid Crystal Elastomers Provide a Path to Biomedical Applications. *J. Appl. Phys.* **2020**, *128*, 140901.
(34) Kotikian, A.; Truby, R. L.; Boley, J. W.; White, T. J.; Lewis, J. A. 3d Printing of Liquid Crystal Elastomeric Actuators with Spatially Programed Nematic Order. *Adv. Mater.* **2018**, *30*, No. 1706164.
(35) Schuhladen, S.; Preller, F.; Rix, R.; Petsch, S.; Zentel, R.; Zappe, H. Iris-Like Tunable Aperture Employing Liquid-Crystal Elastomers. *Adv. Mater.* **2014**, *26*, 7247−7251.
(36) Ditter, D.; Bluemler, P.; Klockner, B.; Hilgert, J.; Zentel, R. Microfluidic Synthesis of Liquid Crystalline Elastomer Particle Transport Systems Which Can Be Remote-Controlled Magnetically. *Adv. Funct. Mater.* **2019**, *29*, No. 1902454.
(37) Zhang, J.; Guo, Y.; Hu, W.; Soon, R. H.; Davidson, Z. S.; Sitti, M. Liquid Crystal Elastomer-Based Magnetic Composite Films for Reconfigurable Shape-Morphing Soft Miniature Machines. *Adv. Mater.* **2021**, *33*, No. 2006191.
(38) Zhang, J.; Guo, Y.; Hu, W.; Sitti, M. Wirelessly Actuated Thermo- and Magneto-Responsive Soft Bimorph Materials with Programmable Shape-Morphing. *Adv. Mater.* **2021**, *33*, 2100336.
(39) Hu, Z. M.; Li, Y. L.; Zhao, T. H.; Lv, J. A. Self-Winding Liquid Crystal Elastomer Fiber Actuators with High Degree of Freedom and Tunable Actuation. *Appl. Mater. Today* **2022**, *27*, No. 101449.
(40) Yakacki, C. M.; Saed, M.; Nair, D. P.; Gong, T.; Reed, S. M.; Bowman, C. N. Tailorable and Programmable Liquid-Crystalline Elastomers Using a Two-Stage Thiol-Acrylate Reaction. *RSC Adv.* **2015**, *5*, 18997−19001.
(41) Zhang, J. Y.; Pang, H. M.; Wang, Y.; Gong, X. L. The Magneto-Mechanical Properties of Off-Axis Anisotropic Magnetorheological Elastomers. *Compos. Sci. Technol.* **2020**, *191*, No. 108079.
(42) Martinoty, P.; Stein, P.; Finkelmann, H.; Pleiner, H.; Brand, H. R. Mechanical Properties of Mono-Domain Side Chain Nematic Elastomers. *Eur. Phys. J. E: Soft Matter Biol. Phys.* **2004**, *14*, 311−321.
(43) Wang, Z.; Xiang, C.; Yao, X.; Le Floch, P.; Mendez, J.; Suo, Z. Stretchable Materials of High Toughness and Low Hysteresis. *Proc. Natl. Acad. Sci. U. S. A.* **2019**, *116*, 5967−5972.
(44) Zhang, J. Y.; Wang, Y.; Pang, H. M.; Sun, S. S.; Xu, Z. B.; Shen, L. J.; Cao, X. F.; Sun, C. L.; Wang, B. C.; Gong, X. L. Flexible Anisotropic Magneto-Sensitive Elastomer Films with out-of-Plane Particle Chain for Bionic Actuator. *Compos. A* **2021**, *150*, No. 106591.

https://doi.org/10.1021/acsapm.3c00858
ACS Appl. Polym. Mater. 2023, 5, 6199−6211